

Star formation activity in the southern Galactic H II region G351.63-1.25

S. Vig,^{1,2*} S. K. Ghosh,^{2,3} D. K. Ojha,² R. P. Verma^{2†} and M. Tamura⁴

¹*Department of Earth and Space Science, Indian Institute of Space Science and Technology, Thiruvananthapuram 695 547, India*

²*Tata Institute of Fundamental Research, Mumbai 400 005, India*

³*National Centre for Radio Astrophysics, TIFR, Pune, 411 007, India*

⁴*National Astronomical Observatory of Japan, Mitaka, Tokyo 181-8588, Japan*

ABSTRACT

The southern Galactic high mass star-forming region, G351.63-1.25, is a H II region-molecular cloud complex with a luminosity of $\sim 2.0 \times 10^5 L_{\odot}$, located at a distance of 2.4 kpc from the Sun. In this paper, we focus on the investigation of the associated H II region, embedded cluster and the interstellar medium in the vicinity of G351.63-1.25. We address the identification of exciting source(s) as well as the census of the stellar populations, in an attempt to unfold star formation activity in this region. The ionised gas distribution has been mapped using the Giant Metrewave Radio Telescope (GMRT), India at three frequencies: 1280, 610 and 325 MHz. The H II region shows an elongated morphology and the 1280 MHz map comprises six resolved high density regions encompassed by diffuse emission spanning $1.4 \times 1.0 \text{ pc}^2$. Based on measurements of flux densities at multiple radio frequencies, the brightest ultra-compact core has electron temperature $T_e \sim 7647 \pm 153 \text{ K}$ and emission measure, $EM \sim 2.0 \pm 0.8 \times 10^7 \text{ cm}^{-6}\text{pc}$. The zero age main-sequence (ZAMS) spectral type of the brightest radio core is O7.5. We have carried out near-infrared observations in the JHK_s bands using the SIRIUS instrument on the 1.4 m Infrared Survey Facility (IRSF) telescope. The near-infrared images reveal the presence of a cluster embedded in nebulous fan-shaped emission. The log-normal slope of the K-band luminosity function of the embedded cluster is found to be $\sim 0.27 \pm 0.03$ and the fraction of the near-infrared excess stars is estimated to be 43%. These indicate that the age of the cluster is consistent with $\sim 1 \text{ Myr}$. Other available data of this region show that the warm (mid-infrared) and cold (millimetre) dust emission peak at different locations indicating progressive stages of star formation process. The champagne flow model from a flat, thin molecular cloud is used to explain the morphology of radio emission with respect to the millimetre cloud and infrared brightness.

Key words: stars: formation – ISM: H II regions – infrared: stars – infrared: ISM – radio continuum: ISM – ISM: individual: G351.63-1.25

1 INTRODUCTION

Our understanding of the formation of massive stars is poor relative to that of low-mass stars (Shu, Adams & Lizano 1987) although considerable progress is being made (Garay & Lizano 1999; Beuther et al. 2007). This is because the formation and early evolution of stars progress deep within the parental molecular cloud of gas and dust. Further adding to the difficulty, is the fast pre-main-sequence evolution of massive stars, their rarity as well as large distances (kpc scale or

larger) as compared to their low mass counterparts. In addition, it has been observed that massive stars usually form in clusters or complexes, i.e. accompanied by swarms of stars of different masses (Testi et al. 1997). The detailed study of massive star-forming complexes necessitates an investigation in different wavelength bands, in order to probe the distinct characteristics of the star formation process. Multi-wavelength observations, therefore, hold the key to unraveling the least understood facets of high-mass star formation.

Star forming complexes in the southern sky have been relatively less studied compared to the northern regions and in this paper we investigate one such star forming region in detail. The massive star-forming region, G351.63-1.25, (associated with IRAS 17258-3637) is a H II region-molecular

* E-mail: sarita@iist.ac.in

† Present address: 301, Vigyan, Plot 23, Sector 17, Vashi, Navi Mumbai 400703, India

cloud complex with a luminosity of $1.9 \times 10^5 L_{\odot}$ (Faúndez et al. 2004). We have adopted a distance of 2.4 kpc based on the studies by Val’tts et al. (2000), Faúndez et al. (2004), and Bik et al. (2005). Millimetre continuum emission from cold dust in this region at 1.2 mm (Faúndez et al. 2004) shows the presence of a single dust core with total mass of $\sim 1400 M_{\odot}$. Culverhouse et al. (2011) have detected emission towards G351.63-1.25 at 2 and 3 mm and this is included in their QUaD Galactic Plane survey catalog. Molecular line investigation of this region has revealed a HC_3N core with tentative CO and SiO outflows (Sollins & Megeath 2004). In the radio continuum, G351.63-1.25 has a very compact source (FWHM $\sim 6''$ at 3.7 cm; Broderick & Brown 1974) which is surrounded by a more extended source (Caswell & Haynes 1987). More recent high resolution radio continuum observations at 8.7 GHz (Walsh et al. 1998) reveal the central region ($6'' \sim 0.07$ pc) to be irregular shaped with local peaks. Ghosh et al. (1990) have presented far-infrared observations of this region in the 120-300 μm band using the Tata Institute of Fundamental Research (TIFR) 100 cm balloon borne telescope. They have constructed a spectral energy distribution from 2 μm to 1 mm and carried out simple radiative transfer calculations using a spherically symmetric dust shell, for an assumed distance of 5 kpc. An infrared cluster located in this region has been discovered by Bica et al. (2003) using the Two-Micron All Sky Survey (2MASS) survey. Further, high resolution K-band spectra of three young stellar objects located in this region have been obtained by Bik et al. (2005); Bik, Kaper & Waters (2006) as a part of their survey to study massive young stellar objects. Methanol maser emission (Slysh et al. 1994; Val’tts et al. 2000), one of the signposts of massive star formation, has also been detected in this region.

While few studies have looked at this massive star-forming region in general, there is no study focussing on the associated embedded cluster. Some of the questions that we aim to address relate to the identification of exciting source(s), census of the stellar populations, and compilation of the available observations to construct a picture of the star formation activity in this region. To carry out this investigation, we have used a combination of infrared and radio wavebands. We probe the young cluster using deeper and high resolution near-infrared (NIR) observations as compared to the previous studies (eg. based on 2MASS). Our new low frequency radio observations of this H II region have the advantage that we can simultaneously image the compact as well as diffuse emission with moderate to high angular resolution.

The layout of the paper is as follows. In Sect. 2, we present the radio and NIR observations as well as a description of other available data-sets used in this study. Sections 3-6 describe the results and in Sect. 7, we discuss the multi-wavelength scenario for star formation in the light of various observational results. The conclusions are presented in Sect. 8.

2 OBSERVATIONS AND DATA REDUCTION

2.1 Radio continuum observations using GMRT

We have carried out low frequency radio continuum observations of G351.63-1.25 at 1280, 610 and 325 MHz using the

Giant Metrewave Radio Telescope (GMRT) located at Khodad, India. The GMRT has a “Y” shaped hybrid configuration of 30 antennas, each of 45 m diameter. Six antennas are placed along each of the three arms (east, west and south) and twelve antennas are located in a random pattern within a compact area $\sim 1 \times 1 \text{ km}^2$ at the centre (Swarup et al. 1991). The baselines ($\sim 100 \text{ m} - 25 \text{ km}$) provide sensitivity to large scale ($\sim 5'$) diffuse emission as well as high angular resolution ($\sim 4 - 20''$). The flux calibrators used during observations were 3C286 & 3C48, and the phase calibrators used were 1626-298, 1822-096 and 1830-360. The details of the radio observations are listed in Table 1.

The National Radio Astronomy Observatory (NRAO) Astronomical Image Processing System (AIPS) was used for data reduction. The data were carefully checked for RF interference and instrumental problems and suitably edited. The calibrated data are Fourier transformed and deconvolved using the IMAGR task in AIPS. Self calibration was carried out to remove the residual effects of atmospheric and ionospheric phase corruptions and obtain the improved maps. In absence of automatic gain control of the antenna system, it becomes important to correct for the system temperature for target sources in the Galactic plane, particularly at lower frequency bands (610 and 325 MHz) where the contribution of sky temperature to system temperature is significant. The fluxes at these frequencies therefore need to be scaled by a factor obtained in the following way. A system temperature for each frequency, T_{corr} , was obtained using the sky temperature towards the target source from the map of Haslam et al. (1982) at 408 MHz. A correction factor, $(T_{corr} + T_{sys})/T_{sys}$, has been used to scale the deconvolved images, where T_{sys} is the system temperature for sources (flux calibrator in our case) away from the Galactic plane. The radio brightness distribution from ionised gas shows a number of high density regions which have been characterised using the task JMFITS (in AIPS). This task fits a 2D-Gaussian function to a selected brightness distribution (having S/N > 10 at 1280 MHz) and gives the position of peaks and the corresponding flux densities.

2.2 Near-infrared observations using IRSF

The region associated with G351.63-1.25 was imaged in the NIR broad bands J (1.25 μm), H (1.63 μm), and K_s (2.14 μm) on 11 July 2004 using the instrument SIRIUS on the 1.4 m InfraRed Survey Facility (IRSF) telescope. SIRIUS is a three-color simultaneous camera equipped with three 1024×1024 HgCdTe arrays. The imaging observations were centered on $\alpha_{2000} = 17^{\text{h}}29^{\text{m}}17^{\text{s}}$, $\delta_{2000} = -36^{\circ}40'13''$. The field-of-view in each band is $\sim 7.8' \times 7.8'$, with a pixel scale of $0.45''$ at the f/10 Cassegrain focus. Further details of the instrument are given in Nagashima et al. (1999) and Nagayama et al. (2003). We obtained 90 dithered frames each of 10s, giving a total integration time of 900s in each band. The observing conditions were photometric and the average FWHM during the observing period was $\sim 1.1'' - 1.4''$. Data reduction was carried out using a software pipeline based on IRAF package tasks. Dome flat-fielding and sky subtraction with a median sky frame were applied. Photometry of point sources was performed using the point spread function (PSF) algorithm ALLSTAR in the DAOPHOT package (Stetson 1987) within the IRAF environment. The PSF

was determined from 20 to 27 relatively bright and isolated stars of the field. For every band (J, H and K_s), we have used an aperture radius of 1 FWHM, with appropriate aperture corrections for the final photometry.

For photometric calibration, we used 21 isolated sources from the 2MASS Point Source Catalog (PSC). The 2MASS covers the sky in the three NIR broad bands J , H and K_s . The sources used for photometric calibration have K_s magnitudes lying in the magnitude range 11-16 and having K_s magnitude errors < 0.1 in all the three, J, H and K_s bands. These 2MASS sources were also used for absolute position calibration and a position accuracy better than $\pm 0.1''$ was achieved. A comparison with 2MASS sources indicates that the brighter IRSF sources with $K_s < 11$ mag are saturated. The magnitudes of these sources were replaced with the corresponding magnitudes from the 2MASS PSC. For comparison with other studies, the magnitudes were transformed to the Bessel and Brett or BB system, (Bessel & Brett 1988) system using the relations given at the 2MASS website¹.

2.3 Other archival datasets

In order to complement our NIR and radio study of this region, we have used the available infrared images and catalog data from the Wide-field Infrared Survey Explorer (WISE), Midcourse Space Experiment (MSX) and Infrared Astronomical Satellite (IRAS) archives, the details of which are given below. The *Spitzer Space Telescope* archive shows that this region has been partially covered using the InfraRed Array Camera (IRAC) in two bands: 4.5 and 8.0 μm . Although of higher angular resolution, these images are saturated near the peak.

2.3.1 WISE

The Wide-field Infrared Survey Explorer (WISE, Wright et al. 2010) mapped the sky at NIR and mid-infrared (MIR) wavebands of 3.4, 4.6, 12, and 22 m ($W1$, $W2$, $W3$ and $W4$ bands, respectively, hereafter) using a 40-cm cryogenically cooled telescope. The angular resolution achieved is $\sim 6''$ at 3.4, 4.6 and 12 μm bands and $\sim 12''$ at 22 μm band (Wright et al. 2010). The region associated with G351.63-1.25 is saturated at the longer MIR wavebands, in $W3$ and $W4$ bands. Hence, for the present study, we have only considered $W1$ and $W2$ bands. The images and catalog sources were taken from the All Sky Data Release².

The catalog sources in the vicinity of G351.63-1.25 have extended source flag of 2 or 3. This indicates that the WISE profile-fit and standard aperture measurements, which are optimized for point sources (with extension flag = 0), systematically underestimate the true flux of these objects and larger aperture photometry is recommended. We have, therefore, carried out aperture photometry anew. A field of size, $10' \times 10'$ centred on $\alpha_{2000} = 17^{\text{h}}29^{\text{m}}16.1^{\text{s}}$, $\delta_{2000} = -36^{\circ}40'7''$, in the WISE bands was considered. The PSF in these bands ($W1$ and $W2$) has been estimated using few bright isolated point sources and is found to be $9''$ and $9.6''$ at $W1$ and $W2$ bands, respectively. The DAOPHOT

library of IDL has been used to carry out aperture photometry. Considering that the field is crowded near the region of interest, we have used aperture and sky annuli of $8''$, $11''$ and $27''$, respectively for both $W1$ and $W2$. The photometry was calibrated with few bright, isolated sources from the WISE catalog.

The sources from the NIR IRSF catalog were compared with those in the WISE catalog by searching for counterparts within $2''$ search radius. This search radius has been selected considering the typical seeing conditions in near-infrared observations. The number of sources having IRSF counterparts in $W1$ and $W2$ bands are 170 and 99, respectively.

2.3.2 MSX

The Midcourse Space Experiment (MSX) surveyed the entire Galactic plane within $|b| \leq 5^\circ$ in four MIR wavebands: 8.3, 12.1, 14.7 and 21.3 μm at a spatial resolution of $\sim 18.3''$ (Price et al. 2001). The panoramic images of the Galactic plane survey of MSX were taken from IPAC (<http://irsa.ipac.caltech.edu/applications/MSX/>). Although of lower angular resolution compared to WISE, the MSX images have been considered because the required coverage of this region at longer wavelengths ($\lambda \geq 8 \mu\text{m}$) is unsaturated and complete. The MSX maps were used to compare the distribution of dust with the ionised gas in this region. Further, point sources in the region associated with G351.63-1.25 have been selected from MSX Point Source Catalog Version 2.3 (Egan, Price & Kraemer 2003).

2.3.3 IRAS-LRS

G351.63-1.25 (as IRAS 17258-3637) appears in the Infrared Astronomical Satellite (IRAS) - Low Resolution Spectrometer (LRS) Catalog (Olton et al. 1986). Our aim in examining the IRAS-LRS spectrum ($8 - 22 \mu\text{m}$) is to ascertain the presence and probe the [Ne II] emission from the ionised gas in this H II region.

3 IONISED GAS DISTRIBUTION

The radio continuum emission maps of the region around G351.63-1.25 obtained for frequencies: 1280, 610 and 325 MHz are shown in Figs. 1 and 2. The synthesized beams and rms noise in these uniformly weighted images are listed in Table 1. The highest resolution map at 1280 MHz has a beam size $7.0'' \times 3.6''$. G351.63-1.25 is well resolved at all the three frequencies and the radio maps show diffuse emission in addition to several high density regions. The total flux densities in the maps up to 3σ level at 1280, 610 and 325 MHz are 10.83 ± 0.06 Jy, 6.11 ± 0.03 Jy and 3.86 ± 0.02 Jy, respectively. The size of the radio emitting gas, based on our interferometric observations ($2.0' \times 1.5' \sim 1.4 \text{ pc} \times 1.0 \text{ pc}$), samples most of the extended emission. This is evident when we compare the size of radio emitting gas from our maps with single dish measurements of this region by Caswell & Haynes (1987) at 5 GHz. These authors used the 64-m Parkes telescope and they detect emission up to $2.5'$.

Six high density ionised regions (compared to the immediate surroundings) have been identified from the map at

¹ www.ipac.caltech.edu/2mass/releases/allsky/doc

² <http://wise2.ipac.caltech.edu/docs/release/allsky/>

1280 MHz. These are labelled as S1, S2, ..., S6 in Fig. 1. At 610 MHz, we see four high density ionised regions (located close to S1, S2, S4 and S6) as compared to six, detected at 1280 MHz. This is likely to be due to a combination of optical thickness effects as well as beam size effects (flux from the point source relative to the diffuse flux in the vicinity) in the images. Details of these regions along with their peak and integrated flux densities at 1280 and 610 MHz are listed in Table 2. In the 325 MHz band, we do not see any point-like source due to poor angular resolution in this band.

3.1 Physical conditions in S2

We have estimated the electron temperature and emission measure of S2 using fluxes at 1280 and 610 MHz by modelling the radio emission to be free-free emission from isothermal, spherically symmetric and homogeneous ionised gas distribution (Mezger & Henderson 1967). Under these approximations, the flux density is given by

$$S_\nu = 3.07 \times 10^{-2} T_e \nu^2 \Omega (1 - e^{-\tau(\nu)})$$

$$\tau(\nu) = 1.643 \times 10^5 a(\nu, T_e) \nu^{-2.1} (EM) T_e^{-1.35}$$

where S_ν is the integrated flux density in Jy, T_e is electron temperature in K, ν is the frequency in MHz, τ is the optical depth, Ω is the solid angle subtended by the source in Steradian (which corresponds to the synthesized beam size for the unresolved core, i.e. $\Omega = 1.33 \theta_x \times \theta_y$ for a gaussian beam), and EM is the emission measure in cm^{-6}pc . The factor $a(\nu, T_e)$ corrects for approximation to the opacity. We take $a(\nu, T_e) = 0.99$ obtained from Table 6 of Mezger & Henderson (1967) for the frequency range 0.6–8 GHz for $T_e = 10,000$ K. In addition to fluxes at 1280 and 610 MHz, we have also used fluxes at 2.7 GHz (Broderick & Brown 1974) and 8.64 GHz (Walsh et al. 1998). They find the presence of a compact H II region (of size $12''$ at 2.7 GHz and $6''$ at 8.64 GHz, respectively). A non-linear least-squares Marquardt-Levenberg algorithm is used to fit the above equation to the flux densities of S2 at four frequencies (0.61, 1.28, 2.7 and 8.64 GHz), after convolving these flux densities to the lowest resolution among the four bands ($12'' \times 12''$). The best-fit model flux densities along with the observed data points are shown in Fig. 3. For this model, the electron temperature and emission measure (with 1σ errors) are 7647 ± 153 K and $2.0 \pm 0.8 \times 10^7 \text{ cm}^{-6}\text{pc}$, respectively. This translates to an electron density $n_e = 1.2 \pm 0.8 \times 10^4 \text{ cm}^{-3}$ for a size of 0.14 pc ($\sim 12''$) assuming constant density. If we consider the flux density at 8.6 GHz by Broderick & Brown (1974) instead, we get a similar T_e value while the electron density is 41% higher. In this paper, we proceed with our former value of n_e . The electron temperature is consistent with $T_e = 7000$ K obtained by Caswell & Haynes (1987) using recombination line measurements. Considering that H II region is 7.4 kpc from the Galactic centre, this value of T_e is in accordance with the variation of electron temperature with Galactocentric distance in ultracompact H II regions, due to a gradual change in the metallicity (Churchwell 2002).

The electron density has been obtained by convolving beams to the lowest resolution beam at 610 MHz. Our high-

est resolution image at 1280 MHz has a beam size corresponding to $\sim 0.08 \text{ pc} \times 0.04 \text{ pc}$. Broderick & Brown (1974) and Walsh et al. (1998) have obtained the bright (small angular scale) component of size 0.07 pc ($\sim 6''$). This implies that n_e is likely to be $> 1.2 \times 10^4 \text{ cm}^{-3}$ in the bright region if we relax the uniform density assumption. The small size and high density imply that it is an ultracompact core embedded within an extended H II component (Kurtz & Franco 2002). In our case, we observe several other high density ionised structures within a more diffuse component. Whether these structures represent a cluster of compact H II regions (each having an embedded exciting source) or high density clumps within the molecular cloud ionised by a single star is discussed in the later sections.

For free-free optically thin emission, the radio flux density is directly proportional to the flux of ionising photons. At 1280 MHz, S2 is optically thick, $\tau \sim 1.5$. Hence, we have used the optically thin flux density at 8.64 GHz (Walsh et al. 1998) to estimate the spectral type of the exciting source. We determine the excitation parameter, U (Schraml & Mezger 1969; Panagia 1973; Jackson & Kraemer 1999) which is given by the expression:

$$U = R_s n_e^{2/3} = 3.6304 [a(\nu, T_e)^{-1} \nu^{0.1} T_e^{0.35} S_\nu d^2]^{1/3}$$

Here, U is in pc cm^{-2} , R_s is the Strömgren radius, d is the distance in kpc. The other terms are same as earlier. The flux of Lyman continuum photons is proportional to U^3 . We obtain $U = 42.3$ which corresponds to a ZAMS star of spectral type O7.5 from the tables of Panagia (1973). The error in flux density leads to a change of $\sim 10\%$ in U that corresponds to a change of < 0.5 in spectral type. For $n_e = 1.2 \times 10^4 \text{ cm}^{-3}$, the Strömgren radius is $R_s = 0.08 \text{ pc}$.

4 EMISSION FROM DUST

The emission from warm dust at $3.4 \mu\text{m}$ WISE image in the vicinity of G351.63-1.25 is shown in Fig. 4 (left). In the image, emission in the form of diffuse filamentary structures is clearly perceived. Although the distributions of diffuse emission at 3.4 and $4.6 \mu\text{m}$ are similar, there is a difference in emission near the peaks. While at $3.4 \mu\text{m}$ we observe a single emission peak, two emission peaks are discerned at $4.6 \mu\text{m}$ shifted to the east. This can be seen in Fig. 4 (right). Note that the emission peaks at 3.4 and $4.6 \mu\text{m}$ are extended and hence point source fluxes would be underestimated using photometry. The MSX survey covers the longer wavelength ($\lambda \geq 8 \mu\text{m}$) MIR region and among the four bands, the best sensitivity is obtained in the $8.3 \mu\text{m}$ band. The diffuse emission in MIR from warm dust at $8.3 \mu\text{m}$ follows a similar trend as the WISE NIR images, albeit with poorer resolution ($\sim 18''$). A strong emission peak is observed at $\alpha_{2000} = 17^h 29^m 16.6^s$, $\delta_{2000} = -36^\circ 40' 15''$. We refer to this as the MSX MIR peak. Another secondary MSX emission peak is detected towards the north-east at $\sim \alpha_{2000} = 17^h 29^m 20^s$, $\delta_{2000} = -36^\circ 39' 35''$. However, the dominant contribution to this peak is from diffuse emission as can be seen by comparison with the WISE images. Integrating the spectral energy distribution of G351.63-1.25, constructed using flux densities (from a circular region of $3'$ around the IRAS peak) from WISE, MSX, IRAS-HIRES maps at 12, 25, 60

and 100 μm (Olson et al. 1986), the IRAS-LRS spectrum, TIFR map at 150 μm (Ghosh et al. 1990) and SIMBA map at 1.2 mm (Faúndez et al. 2004), the total luminosity comes out to be $2 \times 10^5 L_{\odot}$.

From the MSX PSC, we find 3 sources within a circular region of $1'$ centered on the radio peak S2. These are listed in Table 3. We have considered only those fluxes where the MSX quality flag is ≥ 2 . The quality flag is based on detection in various bands and the signal-to-noise ratio. These sources are marked on the 3.4 μm WISE image in Fig. 4 (left) and labelled as M1, M2 and M3. M2 has the largest flux density and corresponds to the MSX MIR peak (mentioned earlier) while M3 corresponds to the secondary MSX peak. M1 and M3 appear to trace the filamentary diffuse structures in the WISE images. This has also been confirmed with the high resolution *Spitzer*-IRAC 8.0 μm image which partially covers this region.

5 EMBEDDED CLUSTER

The NIR images from IRSF have been used to investigate the embedded stellar cluster in this region. The JHK_s colour-composite image of G351.63-1.25 region is shown in Fig. 5. The colour-composite image shows fan-shaped nebular emission apart from a number of point sources. There is a sharp drop in diffuse intensity towards the lower edge of the fan-shaped emission and the reduction in number of point sources is prominent. Further south, faint diffuse emission can be discerned pointing towards the presence of a high extinction ridge. We also notice diffuse emission towards the north-east (top left corner).

5.1 Nature of Stellar sources

In order to study the stellar populations towards this region, we have constructed the colour-magnitude (CM: $J - H$ vs. J) and colour-colour (CC: $H - K$ vs. $J - H$) diagrams. For this, we have considered point sources within a circular region of radius $1.3'$ (~ 0.9 pc) centered on the IRAS peak ($\alpha_{2000} = 17^{\text{h}} 29^{\text{m}} 16.7^{\text{s}}$, $\delta_{2000} = -36^{\circ} 40' 13''$). The circle enclosing this region is shown in Fig. 5 (larger circle). This radius has been selected based on the fact that this circular region encompasses the radio, millimetre and most of the MIR and NIR diffuse emission. We have found a total of 637 K_s band point sources within this circular region, 261 of which are detected in all the three J , H and K_s bands and having errors less than 0.1 mag. The CM and CC diagrams of this sample of 261 sources are shown in Fig. 6. In the CC diagram, the loci of the main-sequence stars, giants, classical T-Tauri stars (Meyer, Calvet & Hillenbrand 1997) and Herbig Ae/Be stars (Lada & Adams 1992) are shown. The reddening vectors of the main-sequence stars, giants, T-Tauri stars are also depicted. All the magnitudes and curves are in the BB system.

We find 61 infrared excess sources which are identified as those lying to the right of the reddening vector drawn from the bottom of the main-sequence curve as well as those lying in the T-Tauri and HeAeBe zones in the CC diagram. These are shown as open circles in the figure. The asterisks represent three young early B or late O type stars whose spectral types have been determined from NIR spectroscopy

by Bik et al. (2005); Bik, Kaper & Waters (2006). They are labelled as IR1 (O9-B1/B1-B2), IR2 (early B) and IR3 (O9-B2) for convenience. The details of their positions, magnitudes and spectral types are given in Table 4. They represent the brightest objects in the cluster. Of these three, only IR1 and IR2 show infrared excess. The rest of the sources in the sample (having no infrared excess or whose spectral types are not known) are represented as dots.

A total of 22 WISE sources have been detected in our circular region of interest, of which 16 have NIR counterparts. We have searched for WISE counterparts to NIR excess sources as well as IR1, IR2 and IR3. Only three NIR excess sources have WISE counterparts, of which one is detected in only $W2$ band of WISE. This is possibly a spurious association since the NIR source is detected in all the three JHK_s bands. We are therefore left with two NIR sources having WISE counterparts. We would like to emphasize here that since the angular resolutions of IRSF and WISE are considerably different ($1''$ and $9''$, respectively), the association is by no means complete. In other words, there are likely to be other NIR excess sources having WISE counterparts but we are unable to isolate them due to the angular resolution and sensitivity of WISE images.

In order to get an estimate of the extinction suffered by these NIR sources, we have dereddened all the sources in the CC diagram along the reddening curve up to a line drawn tangentially to the turn-off point of the main-sequence locus, shown by the long-dashed line in Fig. 6 (right). A histogram of these extinctions shows two marked peaks: the first set ranging from $A_V \sim 0 - 8$ mag and peaking at $A_V = 0$ mag and the second set ranging from $A_V \sim 9 - 20$ mag (peak ~ 10 mag) with few sources having extinction beyond 30 magnitudes. These two distributions are very likely to represent the foreground sources and the cluster, respectively.

5.2 K_s band luminosity function

The K_s band luminosity function (KLF) has been constructed and analysed for the embedded cluster associated with G351.63-1.25. The KLF can be written as a power law of the form

$$\frac{dN(K_s)}{dK_s} \propto 10^{\alpha K_s}$$

where $\frac{dN(K_s)}{dK_s}$ represents the number of stars per unit magnitude bin in K_s and α is the slope of the power law. In order to obtain the KLF, it is important to get an estimate of the foreground and background sources (i.e. sources not associated with the cluster). An estimate of this contamination has been obtained using simulated model counts as well as counts from a nearby control field. For the simulated model counts, we used the Besançon model of population synthesis (Robin et al. 2003). The star counts in the direction $l = 351.6^{\circ}$, $b = -1.3^{\circ}$ were synthesized using stars in the thin disk, thick disk, stellar halo and outer bulge. The fraction of foreground sources in various K_s magnitude bins have been obtained using $A_V = 0$ mag for distances $d < 2.4$ kpc. For the background contribution, we have used model counts assuming $A_V = 20$ mag and $d > 2.4$ kpc. $A_V = 20$ mag has been considered based on the observations that the extinction in the cluster region is $A_V \sim 10 - 20$ mag. The fraction of foreground and background sources

with respect to the total number of stars (determined from the model) was multiplied with star counts in the control field to get a more accurate estimation of the contamination in the cluster region. This is because the number of background sources as estimated from the control field would not have suffered extinction due the nebulous region in this star forming region, G351.63-1.25. This has, therefore, been corrected by using the simulations. The control field has been selected to be a circular region to the west of the nebula, and centered on $\alpha_{2000} = 17^h 29^m 04.15^s$, $\delta_{2000} = -36^\circ 40' 30.3''$. The background and foreground contamination as estimated from the control field is subsequently subtracted from the cluster region in order to obtain the KLF. The KLF of the embedded cluster is shown in Fig. 7 (left) along with the luminosity function without background and foreground correction. We have also estimated the completeness limit of the K_s band by adding artificial stars in the observed image. The observations are complete (90%) to the level of 16.0 mag in this band.

The logarithm of the number of stars as a function of the K_s magnitude for the embedded cluster in this region is shown in Fig. 7 (right). We have fitted a linear function to the $\log(N)$ versus K_s distribution using least-squares method. The best-fit power law is shown as a solid line in Fig. 7 (right). We find $\alpha = 0.27 \pm 0.03$ for the cluster using the K_s magnitude bins 11.5 - 16 mag with a bin-size of 0.5 mag. The fitting has been carried out after taking into consideration, the statistical error on the number of stars in each bin. The value of the power law slope is lower than the typical values (0.32 - 0.38) for other young clusters (Lada, Young & Greene 1993; Carpenter et al. 1993). However, it has been found that for very young clusters with pre-main-sequence objects, the KLF slope is flatter. For instance, Ojha et al. (2004b) have obtained α to be ~ 0.28 for NGC 7538, whose age is estimated to be ~ 1 Myr. Some examples of embedded clusters where even lower values of slope have been reported are: W3-IRS5 (0.18 and 0.17 by Megeath et al. 1996; Ojha et al. 2004a, respectively) with an estimated age of ~ 0.3 Myr. Another example is the case of ρ Ophiucus dark cloud (0.17; Greene & Young 1992) with ages ranging from 0.1 - 1 Myr.

5.3 Mass spectrum and Age estimate

The slope of the KLF is expected to increase with age (Greene & Young 1992). The KLF slope can, therefore, be used as an age indicator. If we assume similar mass-to-luminosity relation as the young cluster NGC 7538 (KLF slope $\alpha = 0.28$, Ojha et al. 2004b), then the age of the young embedded cluster in G351.63-1.25 region ($\alpha = 0.27$) is consistent with ~ 1 Myr. The slope of the initial mass function (IMF), γ , is related to the slope of KLF, α , through the slope of mass-to-luminosity relation β as $\alpha = \gamma/(2.5\beta)$ (Megeath et al. 1996), and hence the IMF slope depends on the value of β used. For $\beta = 1$ (Simon et al. 1992; Lada, Young & Greene 1993), we get $\gamma = 0.68$. However, $\beta = 1$ is used mostly for stars at the lower mass end of the IMF, i.e. G - M stars for a 1 Myr cluster (Megeath et al. 1996). If we use $\beta = 2$, generally used for a larger and higher mass range (O - F stars) at 1 Myr (Balog et al. 2004), then we get $\gamma = 1.35$. This matches the standard Salpeter IMF which is given by $\gamma = 1.35$. A shallower value of β gives a flatter slope. A

literature search shows that for a 1 Myr cluster associated with NGC 7538, Balog et al. (2004) obtain a steeper value of $\gamma \sim 1.58$ using $\beta = 2$. For younger and older populations within the same cluster, i.e. NGC 7538, Ojha et al. (2004b) obtained $\alpha = 0.27 - 0.33$. This yields $\gamma = 1.35 - 1.65$, if we consider $\beta = 2$. Another example is that of 1 Myr Trumpler clusters in Carina Nebula, where $\gamma = 1.30 - 1.40$ has been obtained (Sanchawala et al. 2007). For younger sub-clusters (0.2-0.3 Myr) associated with Sh 2-233IR, flatter slopes of IMF ($\gamma \sim 0.5$) have been obtained, (Yan et al. 2010). Given that the slope of the KLF of G351.63-1.25 is similar to clusters of age 1 Myr for a given mass-to-luminosity relation, we can say that the embedded cluster associated with G351.63-1.25 is very young in nature, whose age is compatible with 1 Myr. It is important to note that this method of age estimation using the luminosity function is an indirect one. The $J - H$ vs. J CM diagram of the cluster field along with the isochrones corresponding to the ages 0.3 Myr and 1 Myr is shown in Fig. 6 (left). The isochrones correspond to those of Palla & Stahler (1999). From Fig. 6 (left), we see that if we consider the 1 Myr isochrone, then the young stellar objects have masses higher than $\sim 0.1 M_\odot$. In other words, our dataset is able to probe young stellar objects of masses up to $\sim 0.1 M_\odot$.

Another age indicator is the fraction of NIR excess stars in a cluster. This is because the disk and/or envelope associated with a pre-main-sequence star starts becoming optically thin with age. This NIR excess fraction method has been used to estimate the ages of young embedded clusters (Lada & Lada 2003). For young clusters whose age is 1 Myr, the fraction of NIR excess stars (based on JHK) is found to be $\sim 50\%$ (Lada et al. 2000; Haisch, Lada & Lada 2000) to $\sim 65\%$ (Muench et al. 2001). In the case of Taurus dark clouds of age 1 - 2 Myr, the NIR fraction is estimated to be $\sim 40\%$ (Kenyon & Hartmann 1995) which decreases to $\sim 20\%$ for older clusters of age 2 - 3 Myr (Teixeira, Lada & Alves 2005). To estimate the NIR excess fraction, it is important to know the contamination in the cluster region due to foreground and background sources. We, again, use the simulated counts from the Besançon model and the star counts in the control field to estimate the fraction of foreground and background contaminating stars, which is 35%. After correcting for the photometric completeness as well as the foreground and background star contamination, the fraction of the NIR excess stars is estimated to be 43% indicating an upper age limit of 1 - 2 Myr. This is compatible with the age estimate obtained earlier by the KLF method.

6 [NE II] EMISSION

The MIR [Ne II] at $12.82 \mu\text{m}$ is a fine-structure line excited by ultraviolet photons of energy > 21.6 eV and hence detection of this line traces far UV photons very close to the young massive star. The [Ne II] line emission along with physical parameters derived from the radio emission can be used to estimate the effective temperature of the ionizing star (Watarai et al. 1998). In the IRAS-LRS spectrum of G351.63-1.25, a strong emission line at $12.8 \mu\text{m}$ corresponding to [Ne II] is observed. The [Ne II] line intensity is $F_{[\text{Ne II}]} \sim 8.2 \times 10^{-17} \text{ W cm}^{-2}$. This has been determined by fitting a gaussian function to the line and integrating

the area under the curve after subtraction of a polynomial baseline.

Although the [Ne II] line is from a wide aperture of $5'$ (corresponding to the IRAS-LRS detectors), we estimate the spectral type of the exciting source assuming that this emission arises due to a single massive star associated with S2. This is because the formalism considered here uses [Ne II] emission due to a single ZAMS star to estimate its effective temperature. The Ne^+ abundance (Ne^+/H^+) is obtained using the following equation for the case when the electron density is below the critical density ($n_{\text{crit}} = 3.6 \times 10^5 \text{ cm}^{-3}$), (Takahashi et al. 2000):

$$\frac{\text{Ne}^+}{\text{H}^+} = \frac{F_{[\text{Ne II}]}}{2.3 \times 10^{-9} \Omega_b T_e^{-1/2} e^{-(hc/\lambda k T_e)} (EM)}$$

where $F_{[\text{Ne II}]}$ is the [Ne II] line flux density, Ω_b is the solid angle of the [Ne II] emitting region in Sr, T_e is the electron temperature in K, λ in the Boltzmann factor is the wavelength of the [Ne II] line ($12.81 \mu\text{m}$ in this case), and EM is the emission measure in $\text{cm}^{-6} \text{ pc}$. The electron density obtained for S2, $n_e = 1.2 \times 10^4 \text{ cm}^{-3}$ is an order of magnitude lower than the critical density. Further, we assume that the spatial distribution of [Ne II] line emission overlaps the compact core of the ionised gas implying $\Omega_b \sim 12''$. For this region, we find Ne^+ abundance to be $\sim 4.5 \times 10^{-5}$. Takahashi et al. (2000) have calculated (and plotted) the Ne^+ abundance as a function of the effective temperature of the ionising star from the H II region model using the *CoStar* stellar atmosphere model of Takahashi et al. (2000). Using this, we find that our Ne^+ abundance corresponds to a stellar effective temperature of $\sim 36000 \text{ K}$, i.e a star of spectral type O8.5-O8. This is later than the spectral type of the ionising star obtained from radio measurements (O7.5). This could be explained on the basis of the size of the Ne^+ emitting region. We have assumed that the size of the [Ne II] emitting region coincides with the compact radio peak. However, it has been found that for the relatively massive stars causing ionisation, the size of the Ne^+ abundance shows a dip at the location of the radio peak, due to larger Ne^{++} abundance (Takahashi et al. 2000). These authors also find that the spectral type of the ionising star obtained from the Ne^+ abundance measurements is 1-2 subclasses later than the spectral type obtained from radio measurements.

7 THE MULTIWAVELENGTH SCENARIO

In this section, we analyse and interpret our results in different wavebands in order to understand various aspects of the star formation process occurring in this region.

7.1 Nature of S2

Among the six ionised clumps listed in Table 2, the brightest is S2 whose excitation is consistent with a ZAMS star of radio spectral type O7.5. The radio morphology of S2 at 1280 MHz is not point-like. This is confirmed from the high angular resolution ($1.5''$) map at 8.64 GHz by Walsh et al. (1998). In their map, S2 displays an irregular morphology comprising near equal intensity five peaks, with a typical separation of $1 - 3''$. Assuming that the emission

is optically thin and each radio peak represents a ZAMS O/B star, this would mean that a cluster of OB stars exist within a region of size 0.07 pc. On the other hand, these could be high density clumps ionised externally. In that case, since they are of nearly equal brightnesses, optical depth must be playing an important role. While the 8.64 GHz map images only the finer details, the 1280 MHz image shows more nebulous components with shoulders in emission ($19'' \times 23'' \sim 0.2 \times 0.3 \text{ pc}^2$). We can therefore consider S2 as an ultracompact H II region inside a compact component which in turn is embedded in a more extended emission component (Kim & Koo 2001).

S2 does not coincide with any known infrared point source within a search radius of $3''$ ($\sim 0.03 \text{ pc}$), as investigated using IRSF and MSX. There is an offset between the radio and MIR peaks. This implies that ionising source(s) is deeply embedded and suffer extinction even in the MIR. This is clearly evident from the WISE images in Fig. 4. This hypothesis (high extinction towards S2) is further validated by the presence of a dense molecular (HC_3N) core (with virial mass upper limit is $940 M_\odot$) by Sollins & Megeath (2004). The source closest to S2 ($3.2''$) in the NIR is a very 'red' source detected in H and K_s bands only ($H - K = 3.52 \text{ mag}$; $K_s = 13.08 \text{ mag}$) which has also been detected at $4.5 \mu\text{m}$. This source is adjacent to the west of a high density filamentary structure running vertically, which is visible in the colour-composite JHK_s image in Fig. 5. The closest star detected in all three JHK_s bands in the vicinity of S2 is located $\sim 6.8''$ away and has NIR extinction larger than $A_V \sim 20 \text{ mag}$. The massive young stellar object, IR2, is at a distance $8.6''$ from the radio peak. Bik, Kaper & Waters (2006) carried out VLT K-band spectroscopy of IR2 (referred as 17258nr593 in their paper) and classified it as an early B star (having 16 magnitudes of visual extinction). IR2 has an infrared excess as seen in the CC diagram. The bright MIR young stellar object detected at $3.4 \mu\text{m}$ WISE and $8.3 \mu\text{m}$ MSX images lies at the western edge of S2 and is probably, responsible for the small shoulder in radio emission seen towards the west of S2 (Fig. 4 left). The presence of massive young stellar objects like IR2, the infrared excess sources as well as the sources detected only in H and K_s bands lends credibility to our hypothesis that S2 is excited by a cluster of embedded young massive objects. The compact ionised component of S2 is therefore being powered by UV photons escaping from the UCHII region as well as by other massive embedded young stellar objects (like IR2). This concurs with the conclusion of Kurtz, Churchwell & Wood (1994) that many ultracompact H II regions are powered by a cluster of stars.

7.2 Do the other ionised clumps harbour stars?

We first search for NIR counterparts to radio peaks (other than S2) within a search radius of $3''$ considering the resolution of radio map at 1280 MHz. We do not find any NIR counterpart to S1, S3, S4 and S6. For S5, the closest NIR source is $0.9''$ away. However, this is neither an infrared excess source nor an early spectral type object (based on the CM diagram). It is very likely to be a foreground source along the same line-of-sight. The young stellar object IR3 is located $\sim 10''$ away from S4. Bik (2004) has also carried out K band spectroscopy of IR3 (17258nr378 in his work)

and infer its spectral type as O9-B2. It appears unlikely to be a massive young star as we do not observe compact radio emission coincident with IR3. Neither do Walsh et al. (1998) find any compact source here. Therefore, the radio emission indicates that the spectral type of IR3 is consistent with B2-B1. The NIR source closest to S4 is $3.7''$ away and detected only in K_s band ($K_s = 15.25$ mag). With the given data, it is difficult to ascertain which young stellar object is responsible for the radio peaks, but it is likely that the more massive ones among these are contributing to the radio emission.

We now explore the hypothesis that these high density ionised regions are externally ionised clumps located in an elongated H II region created by a group of young massive stars located in S2. Note that the peak flux densities are lower than that of S2 by a factor of 5 or more. The flux densities at the location of these clumps based on solid angle subtended by them from the ionising star(s) are estimated. For clumps other than S5, the derived values are much lower than observed flux densities (7-30%). For S5, this ratio is higher $\sim 80\%$. This would imply that most of these ionised clumps have an embedded ZAMS exciting star. However, this result must be treated with caution as there are two opposing factors that have been ignored here. First, these estimates were obtained assuming an absence of intervening medium, in which case the ratios would go lower. On the other hand, we have assumed optically thin emission, for S2 as well as the ionised clumps. However, we have seen that S2 is optically thick and high optical depth for the other clumps cannot be ruled out. Consequently, the flux densities cannot be compared directly and a map with optically thin emission from all the clumps would enable a better comparison. In addition, we do not find NIR counterparts to these ionised clumps; and the morphology of the ionised clumps are relatively less compact, with the exception of S3 and S5. At higher radio frequencies, the emission from these clumps are resolved out at by an extended array configuration (Walsh et al. 1998). These could, therefore, be more evolved individual H II regions in case they harbour stars. However, since we do not observe the associated exciting stars in infrared, we are inclined to take the view that these are high density clumps in the extended emission of the ultracompact H II region.

7.3 Star formation activity

The radio continuum emission at 1280 and 610 MHz traces extended as well as compact emission in the region associated with G351.63-1.25. The extended emission from ionised gas is elongated along the northeast-southwest direction. On both sides of the elongated emission, we observe steep gradients in brightness distribution. This signifies that this region is ionisation bounded on both sides suggesting an encounter with the ambient molecular gas during the expansion phase of the H II region. If we compare the morphology of the diffuse emission in the radio and MIR, we perceive that the radio contours follow the MIR diffuse emission from warm dust. This is clearly visible in Fig. 4 (left) towards the north of S2 as well as along the elongation. Although not shown here, the high resolution $8.0 \mu\text{m}$ *Spitzer*-IRAC image (which covers only the northern part of this diffuse emission) resolves the diffuse emission into filamentary structures. High

extinction filamentary structures are also seen in the NIR images entwined with the nebulous emission. This indicates that this region is highly inhomogeneous implying a variation in extinction.

The emission from cold dust at 1.2 mm from Faúndez et al. (2004) is shown in Fig. 8 (right) as contours. The millimetre emission shows a core with peak flux of 13.8 Jy/beam, where the beam size is $24''$. The total mass of this cold core estimated from millimetre emission is $1400 M_{\odot}$. A core dust temperature of 42 K is obtained based on a grey body fit to the fluxes at the far-infrared wavelengths by Faúndez et al. (2004). The dust optical depth at 1.2 mm is estimated to be 3.7×10^{-3} which translates to an optical depth of 0.3 at $100 \mu\text{m}$ if we consider the extinction from silicate grains of Mathis, Mezger & Panagia (1983). This region has been detected as a compact core in the 2 and 3 mm QUaD survey (Culverhouse et al. 2011) with flux densities 37.6 ± 0.3 (beam $\sim 3.8' \times 1.8'$) and 30.9 ± 0.2 Jy (beam $\sim 4.0' \times 2.3'$), respectively. While the 3 mm emission has non-negligible contribution from the free-free emission to the dust emission, we assume this is not the case for the 2 mm emission. It is difficult to estimate the mass of such a cold clump, using the 2 mm emission, as the values of dust temperature and opacity are not known accurately. If we extrapolate the formalism of Hildebrand (1983) to millimetre wavelengths, we get the dust opacity as $\kappa_{2\text{mm}} = 0.01 \text{ g/cm}^2$. This leads to a dust mass of $360 M_{\odot}$ for a dust temperature of 30K. This is an order of magnitude larger than the mass of dust emitting at 1.2 mm (Faúndez et al. 2004). Considering that the resolution is poorer at 2 mm, it is likely that other cold clumps in the vicinity could be contributing to this emission. A comparison of the morphology of the warm and cold dust distributions from MIR and 1.2 mm maps respectively, shows that the emission at different wavebands peak at different locations. The millimetre emission peaks at $(\alpha_{2000}, \delta_{2000}) = (17^{\text{h}} 29^{\text{m}} 18.11^{\text{s}}, -36^{\circ} 40' 21.0'')$ towards the south-east ($\sim 20''$) of the peak emission from warm dust and ionised gas (separation $\sim 19''$). This is evident from Fig. 8 (right).

A search for masers in this region shows that a methanol maser has been detected here (Slysh et al. 1994; Val'tts et al. 2000). The triangle in Fig. 8 (right) shows the location of the peak methanol maser emission. This is a Class I methanol maser detected at 44 and 95 GHz. Kurtz, Hofner & Álvarez (2004) find a large number of these masers in relatively close association with other massive star formation signposts like water masers and H II regions. In their VLA survey of star-forming regions, they find that these masers are typically offset by ~ 0.2 pc (median value) from the star formation signposts. In the case of G351.63-1.25, the maser is offset from the peak radio emission by 0.2 pc ($\sim 14''$). It is believed that Class I masers are associated with shock fronts, indicating the interface of interaction between mass outflows and dense ambient material (Plambeck & Menten 1990). Note that the observations of Sollins & Megeath (2004) point towards tentative detection of CO and SiO outflows from this region. The shock front exciting the maser is probably due to the interface (along the elongation) of the ionised gas/outflow and the cold millimetre clump. The absence of radio and infrared emission peaks near the millimetre emission peak indicates that formation of stars is either in a very early stage or has not yet begun.

The investigation of G351.63-1.25 at different wavelength bands ranging from NIR to millimetre wavelengths, leads to the following scenario. Based on evidences relating to (a) morphology of S2, (b) absence of infrared source corresponding to S2 peak position, (c) presence of young stellar objects within nebulosity of S2 (d) detection of a dense molecular gas (HC_3N) core close to S2 (e) presence of Class I methanol maser, and (f) tentative detection of CO and SiO outflows, we can say that the G351.63-1.25 comprises a group of embedded massive young stellar objects responsible for ionisation of the compact source S2. Regarding other ionised clumps, we are inclined to take the view that these are externally ionised by the central cluster, based on (a) absence of infrared counterparts, and (b) optical depth effects. Further high frequency radio observations, sampling emission from the ionised clumps, are needed in order to ascertain that they host massive stars.

The morphology of the H II region is elongated with ionisation bounds on either side of the elongation and density bounds along the elongation direction, similar to a bipolar H II region (Kim & Koo 2001; Felli et al. 1984). Note that the elongation is perpendicular to the direction of the line joining S2 and the millimetre peak, shown by dashed line in Fig. 8 (right). Further, the millimetre cloud is elongated in this direction (dashed line). This suggests that the molecular cloud is dense along this direction with massive stars being formed here, vis-a-vis S2. The peak brightnesses at 3.4 and 4.6 μm due to warm dust also lie in this direction lending support to this hypothesis. We propose a scenario where the star formation proceeds in the flat molecular cloud while the expansion of the H II region occurs away from it, in a direction perpendicular to the molecular cloud. Multiwavelength observations indicate the presence of massive stars, cold dust emitting millimetre emission as well as hot dust emitting near- and mid-infrared emission in this flat molecular cloud. As these lie at different locations within the flat molecular cloud, it implies that G351.63-1.25 is a region that displays different evolutionary stages of star formation.

The bipolar radio morphology in extended emission can be explained in terms of the champagne flow model (Israel 1978; Tenorio-Tagle 1979). The champagne flow model explains the shape of a H II region to be due to the density gradient of the molecular material in the vicinity of the newly formed massive star. The present scenario of flat molecular cloud has been modelled by Bodenheimer, Tenorio-Tagle & Yorke (1979) where the ionisation front breaks out through two opposing faces of the same cloud. A star located within a disk-like flat molecular cloud produces an H II region which breaks through the cloud in both directions in a double cone-like structure, the opening angle of which widens over time. In the case of G351.63-1.25, if we assume that the exciting cluster of stars is located in a thin, flattened molecular cloud (indicated by the millimetre cloud, infrared peaks and maser spot), then the expansion of the H II region would lead to a bipolar type of morphology in a direction perpendicular to the flat cloud as the density gradient is maximum here. The high density ridge (towards the lower part of the fan-shaped nebulous region) is roughly in the same direction as the flat molecular cloud (dashed line in Fig. 8 (right)). If this is part of the same thin, flat molecular cloud, then the geometry implies that the thin cloud is not fully edge-on (i.e. inclination angle $< 90^\circ$) to our line-of-sight. This would also explain the

asymmetry in length of the lobes of the H II region. However, high angular resolution molecular line imaging observations of the ambient molecular cloud will be required to confirm this.

8 CONCLUSIONS

Based on the multiwavelength (radio, infrared and millimetre) investigation of the star-forming region associated with G351.63-1.25 presented here, we come to the following conclusions.

(i) The radio map of the H II region at 1280 MHz comprises of six high density ionised clumps embedded in diffuse emission. The brightest clump at S2 is an ultracompact H II region with the electron temperature $\sim 7647 \pm 153$ K and emission measure $\sim 2.0 \pm 0.8 \times 10^7 \text{ cm}^{-6} \text{ pc}$. The equivalent ZAMS spectral type is estimated to be O7.5.

(ii) The NIR broad band images in J, H and K_s reveal the presence of fan-shaped nebulous emission as well as high extinction filamentary structures. The stellar component is probed using colour-magnitude and colour-colour diagrams. These have been used to find the infrared excess sources, associated with the embedded cluster. The log-normal slope of the KLF of the embedded cluster after removing the contamination due to foreground and background sources is $\sim 0.27 \pm 0.03$, indicating the youth of the cluster. The fraction of the NIR excess stars is estimated to be 43% indicating an upper age limit of 1 - 2 Myr. Based on KLF as well as NIR excess fraction, we believe that age of the cluster is compatible with ~ 1 Myr.

(iii) The MIR images from WISE and MSX show diffuse emission that matches the ionised gas distribution very well.

(iv) The ultracompact component S2, does not have an infrared counterpart within $3''$ of the radio peak at 1280 MHz. Further, based on the morphology of S2 (not point-like), the presence of other young stellar objects within the nebulosity of S2, the detection of dense molecular gas core close to it, the presence of Class I methanol maser as well as tentative evidence of SiO outflows, it is very likely that S2 is ionised by a group of massive embedded sources rather than a single source.

(v) The ionised clumps seen in the 1280 MHz map are likely to be externally ionised by the central cluster associated with S2 due to absence of NIR counterparts, less compact morphology, and optical depth effects at 1280 and 610 MHz.

(vi) The warm and cold dust distributions (from MIR and millimetre emission) peak at different locations. The ionised emission is elongated indicating ionisation bounds on either side. The elongation is perpendicular to the direction of the line joining the peak brightness of ionised gas and cold dust. This is explained using the champagne flow model where star formation occurs in a thin, flat molecular cloud and the expansion of the H II region happens away from the cloud leading to a bipolar-type morphology of extended emission.

ACKNOWLEDGEMENTS

We thank the staff of the GMRT, who have made the radio observations possible. GMRT is run by the National Centre

for Radio Astrophysics of the Tata Institute of Fundamental Research. We also thank the staff of IRSF at S. Africa in joint partnership between the S.A.A.O and Nagoya University of Japan for their assistance and support during observations. We thank L. Bronfman for providing us the 1.2 mm map of this region. We thank Anne Robin for letting us use her model of stellar population synthesis.

We thank IPAC, Caltech, for providing us the HIRES-processed IRAS products. This research made use of data products from the Midcourse Space Experiment. Processing of the data was funded by the Ballistic Missile Defense Organization with additional support from NASA Office of Space Science. This research has also made use of the NASA/ IPAC Infrared Science Archive, which is operated by the Jet Propulsion Laboratory, Caltech, under contract with the NASA. This publication makes use of data products from the Wide-field Infrared Survey Explorer, which is a joint project of the University of California, Los Angeles, and the Jet Propulsion Laboratory/California Institute of Technology, funded by the National Aeronautics and Space Administration.

REFERENCES

- Balog Z., Kenyon S. J., Lada E. A., Barsony M., Vinkó J., Gáspár A., 2004, *AJ*, 128, 2942
- Bessell M. S., Brett J. M., 1988, *PASP*, 100, 1134
- Beuther H., Churchwell E. B., McKee C. F., Tan J. C., 2007, *Protostars and Planets V*, 165
- Bica E., Dutra C. M., Soares J., Barbuy B., 2003, *A&A*, 404, 223
- Bik A., 2004, PhD Thesis, Astronomical Institute Anton Pannekoek, University of Amsterdam
- Bik A., Kaper L., Hanson M. M., Smits M., 2005, *A&A*, 440, 121
- Bik A., Kaper L., Waters L. B. F. M., 2006, *A&A*, 455, 561
- Bodenheimer P., Tenorio-Tagle G., Yorke H. W., 1979, *ApJ*, 233, 85
- Broderick J. J., Brown R. L., 1974, *ApJ*, 192, 343
- Carpenter J. M., Snell R. L., Schloerb F. P., Skrutskie M. F., 1993, *ApJ*, 407, 657
- Caswell J. L., Haynes R. F., 1987, *A&A*, 171, 261
- Churchwell E., 2002, *ARA&A*, 40, 27
- Culverhouse T. et al., 2011, *ApJS*, 195, 8
- Egan M. P., Price S. D., Kraemer K. E., 2003, in *Bulletin of the American Astronomical Society*, Vol. 35, American Astronomical Society Meeting Abstracts, p. 1301
- Faúndez S., Bronfman L., Garay G., Chini R., Nyman L.-Å., May J., 2004, *A&A*, 426, 97
- Felli M., Massi M., Staude H. J., Reddmann T., Eiroa C., Hefele H., Neckel T., Panagia N., 1984, *A&A*, 135, 261
- Garay G., Lizano S., 1999, *PASP*, 111, 1049
- Ghosh S. K., Iyengar K. V. K., Rengarajan T. N., Tandon S. N., Verma R. P., Daniel R. R., 1990, *ApJ*, 353, 564
- Greene T. P., Young E. T., 1992, *ApJ*, 395, 516
- Haisch, Jr. K. E., Lada E. A., Lada C. J., 2000, *AJ*, 120, 1396
- Haslam C. G. T., Salter C. J., Stoffel H., Wilson W. E., 1982, *A&AS*, 47, 1
- Hildebrand R. H., 1983, *QJRAS*, 24, 267
- Israel F. P., 1978, *A&A*, 70, 769
- Jackson J. M., Kraemer K. E., 1999, *ApJ*, 512, 260
- Kenyon S. J., Hartmann L., 1995, *ApJS*, 101, 117
- Kim K.-T., Koo B.-C., 2001, *ApJ*, 549, 979
- Kurtz S., Churchwell E., Wood D. O. S., 1994, *ApJS*, 91, 659
- Kurtz S., Franco J., 2002, in *Revista Mexicana de Astronomía y Astrofísica Conference Series*, Vol. 12, *Revista Mexicana de Astronomía y Astrofísica Conference Series*, Henney W. J., Franco J., Martos M., eds., pp. 16–21
- Kurtz S., Hofner P., Álvarez C. V., 2004, *ApJS*, 155, 149
- Lada C. J., Adams F. C., 1992, *ApJ*, 393, 278
- Lada C. J., Lada E. A., 2003, *ARA&A*, 41, 57
- Lada C. J., Muench A. A., Haisch, Jr. K. E., Lada E. A., Alves J. F., Tollestrup E. V., Willner S. P., 2000, *AJ*, 120, 3162
- Lada C. J., Young E. T., Greene T. P., 1993, *ApJ*, 408, 471
- Mathis J. S., Mezger P. G., Panagia N., 1983, *A&A*, 128, 212
- Megeath S. T., Herter T., Beichman C., Gautier N., Hester J. J., Rayner J., Shupe D., 1996, *A&A*, 307, 775
- Meyer M. R., Calvet N., Hillenbrand L. A., 1997, *AJ*, 114, 288
- Mezger P. G., Henderson A. P., 1967, *ApJ*, 147, 471
- Muench A. A., Alves J., Lada C. J., Lada E. A., 2001, *ApJ*, 558, L51
- Nagashima C. et al., 1999, in *Star Formation 1999*, T. Nakamoto, ed., pp. 397–398
- Nagayama T. et al., 2003, in *Society of Photo-Optical Instrumentation Engineers (SPIE) Conference Series*, Vol. 4841, *Society of Photo-Optical Instrumentation Engineers (SPIE) Conference Series*, M. Iye & A. F. M. Moorwood, ed., pp. 459–464
- Ojha D. K. et al., 2004a, *ApJ*, 608, 797
- Ojha D. K. et al., 2004b, *ApJ*, 616, 1042
- Olson F. M. et al., 1986, *A&AS*, 65, 607
- Palla F., Stahler S. W., 1999, *ApJ*, 525, 772
- Panagia N., 1973, *AJ*, 78, 929
- Plambeck R. L., Menten K. M., 1990, *ApJ*, 364, 555
- Price S. D., Egan M. P., Carey S. J., Mizuno D. R., Kuchar T. A., 2001, *AJ*, 121, 2819
- Robin A. C., Reylé C., Derrière S., Picaud S., 2003, *A&A*, 409, 523
- Sanchawala K. et al., 2007, *ApJ*, 667, 963
- Schraml J., Mezger P. G., 1969, *ApJ*, 156, 269
- Shu F. H., Adams F. C., Lizano S., 1987, *ARA&A*, 25, 23
- Simon M., Chen W. P., Howell R. R., Benson J. A., Slowik D., 1992, *ApJ*, 384, 212
- Slysh V. I., Kalenskii S. V., Val'tts I. E., Otrupcek R., 1994, *MNRAS*, 268, 464
- Sollins P. K., Megeath S. T., 2004, *AJ*, 128, 2374
- Stetson P. B., 1987, *PASP*, 99, 191
- Swarup G., Ananthakrishnan S., Kapahi V. K., Rao A. P., Subrahmanya C. R., Kulkarni V. K., 1991, *CURRENT SCIENCE* V.60, NO.2/JAN25, P. 95, 1991, 60, 95
- Takahashi H., Matsuhara H., Watarai H., Matsumoto T., 2000, *ApJ*, 541, 779
- Teixeira P. S., Lada C. J., Alves J. F., 2005, *ApJ*, 629, 276
- Tenorio-Tagle G., 1979, *A&A*, 71, 59
- Testi L., Palla F., Prusti T., Natta A., Maltagliati S., 1997, *A&A*, 320, 159
- Val'tts I. E., Ellingsen S. P., Slysh V. I., Kalenskii S. V., Otrupcek R., Larionov G. M., 2000, *MNRAS*, 317, 315

- Walsh A. J., Burton M. G., Hyland A. R., Robinson G.,
1998, MNRAS, 301, 640
Watarai H., Matsuhara H., Takahashi H., Matsumoto T.,
1998, ApJ, 507, 263
Wright E. L. et al., 2010, AJ, 140, 1868
Yan C.-H., Minh Y. C., Wang S.-Y., Su Y.-N., Ginsburg
A., 2010, ApJ, 720, 1

Table 1. Details of the radio continuum observations carried out for G351.63-1.25 using the GMRT, India.

Frequency band (MHz)	1280	610	325
Date of Observation	29 Oct 2001	22 June 2000	04 Oct 2003
Primary beam	26'.2	54'	1°.8
Synthesized beam	7.0'' × 3.6''	11.7'' × 8.0''	36.8'' × 16.2''
Map noise (mJy/beam)	2	2	3
Continuum bandwidth	16 MHz	16 MHz	16 MHz
Flux Calibrator	3C286, 3C48	3C48	3C286, 3C48
Phase Calibrator	1626-298	1822-096	1830-360

Table 2. List of extracted sources along with their peak and integrated flux densities obtained from the radio maps of G351.63-1.25 at 1280 and 610 MHz.

Source No.	RA (J2000) (h m s)	Dec (J2000) (° ' ")	1280 MHz		610 MHz	
			Peak Flux (mJy/bm)	Int flux (mJy)	Peak Flux (mJy/bm)	Int flux (mJy)
S1	17 29 16.42	-36 40 38.0	36.0 ± 4.5	372.7 ± 51.4	56.6 ± 2.6	245.8 ± 13.7
S2	17 29 16.77	-36 40 10.4	326.5 ± 3.4	5894.3 ± 65.1	238.6 ± 2.6	2345.0 ± 27.6
S3	17 29 17.52	-36 40 49.4	23.5 ± 4.6	167.8 ± 37.6	-	-
S4	17 29 19.61	-36 39 37.4	59.3 ± 3.9	846.7 ± 59.0	105.9 ± 2.6	799.3 ± 21.8
S5	17 29 19.91	-36 39 50.0	23.9 ± 4.7	148.6 ± 33.4	-	-
S6	17 29 20.96	-36 39 44.0	28.4 ± 4.3	359.9 ± 59.3	58.5 ± 2.6	336.6 ± 17.3

Table 3. Details of MSX PSC sources in the region associated with G351.63-1.25.

MSX PSC designation	Name ^a	α_{2000} (deg)	δ_{2000} (deg)	F_8 (Jy)	F_{12} (Jy)	F_{14} (Jy)	F_{21} (Jy)
G351.6423-01.2409	M1	262.3143	-36.6560	2.8 ± 0.1	4.1 ± 0.2	-	-
G351.6326-01.2523	M2	262.3195	-36.6704	28.0 ± 0.1	97.1 ± 4.9	166.1 ± 10.1	778.8 ± 46.7
G351.6469-01.2554	M3	262.3325	-36.6602	8.8 ± 0.4	23.8 ± 1.2	28.7 ± 1.7	130.0 ± 7.8

^a Short name used in the present work**Table 4.** Details of the IRSF-SIRIUS sources in the G351.63-1.25 region with known spectral types based on near-infrared spectroscopic studies by Bik et al. (2005) and Bik, Kaper & Waters (2006).

Source Name	$\alpha_{(2000)}$ (deg)	$\delta_{(2000)}$ (deg)	J (mag)	H (mag)	K_s (mag)	Spectral Type
IR1	262.30841	-36.67229	12.46 ± 0.02	11.24 ± 0.03	10.49 ± 0.04	O9-B1/B2-B3
IR2	262.31714	-36.66863	13.91 ± 0.03	11.19 ± 0.05	9.21 ± 0.04	early B
IR3	262.33078	-36.65780	13.29 ± 0.03	11.11 ± 0.03	10.05 ± 0.03	O9-B2

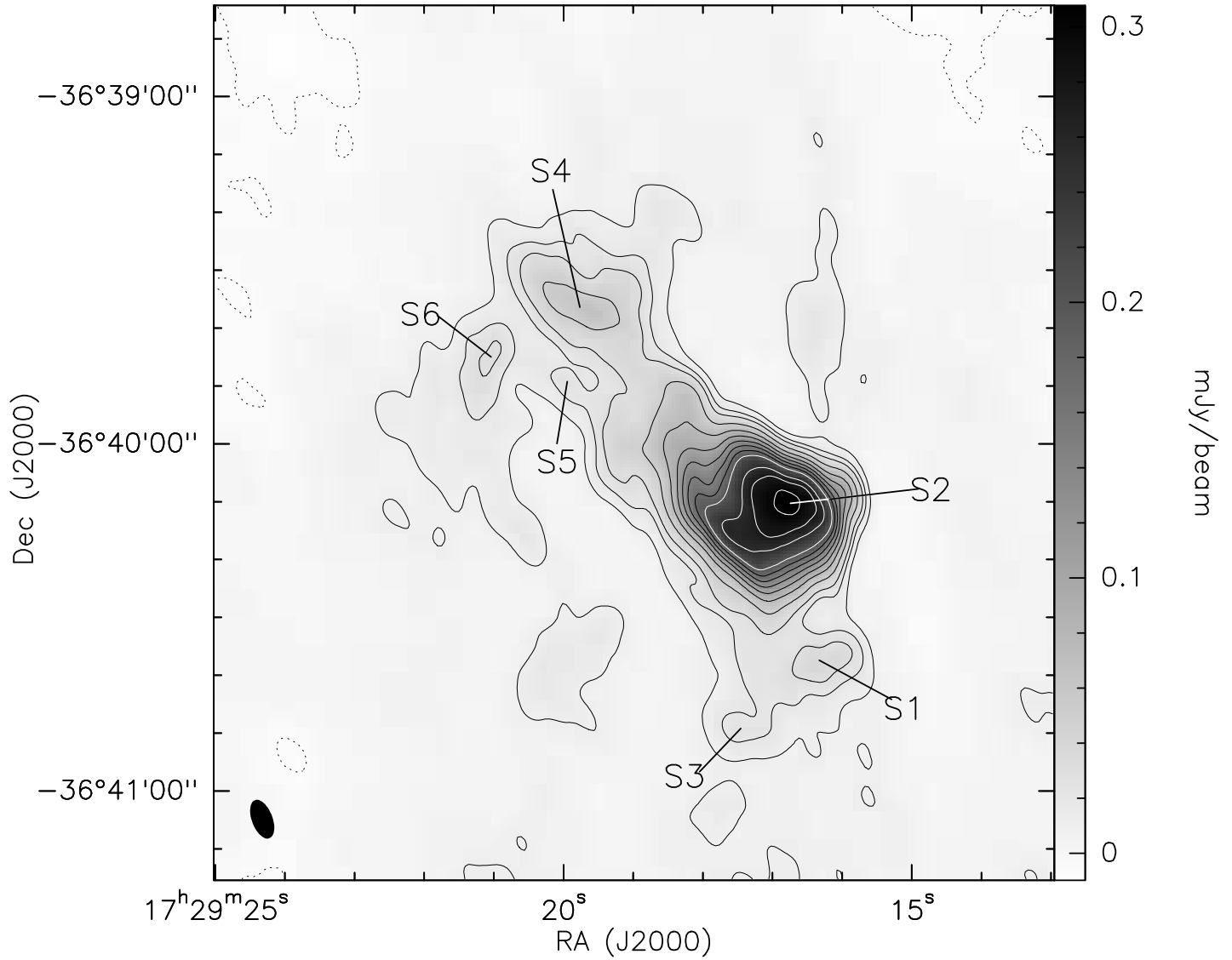


Figure 1. Radio continuum emission at 1280 MHz in the region around G351.63-1.25. The contour levels are at -5, 10, 20, 30, 50, 75, 100, 125, 150, 175, 200, 250, 275 and 300 mJy/beam. The negative contour is indicated by a dotted line. The discrete radio sources are represented by the numbers as listed in Table 2. The beam size is 7.0" × 3.6" (shown as dark ellipse in the lower left corner of the figure) and the rms noise is 2 mJy/beam.

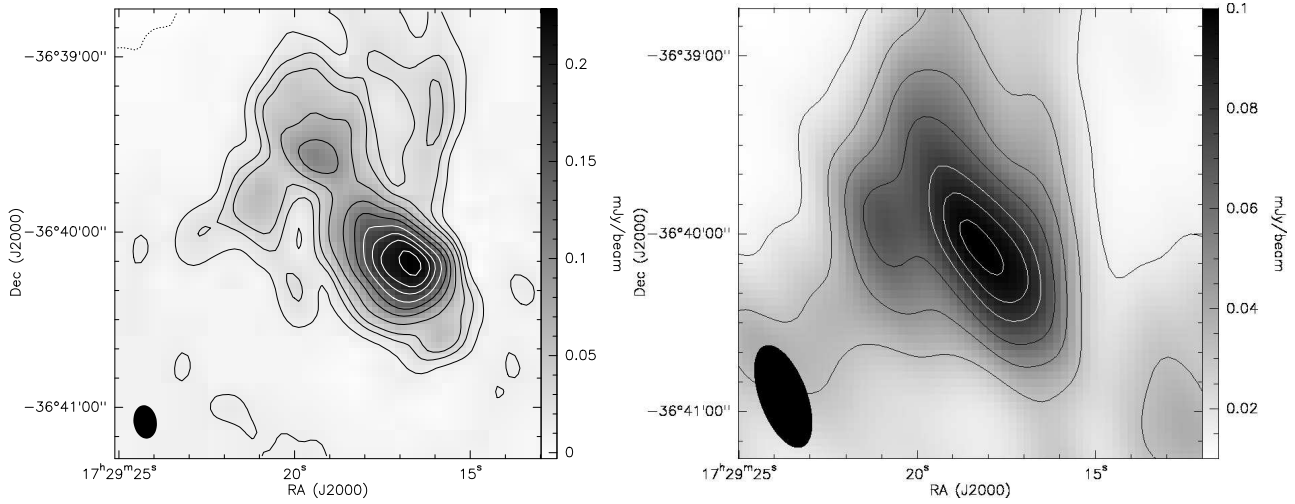


Figure 2. Radio continuum emission at 610 (left) and 325 MHz (right) in the region around G351.63-1.25. The contour levels are at -1, 12, 24, 36, 60, 90, 120, 150, 180, 200 and 220 mJy/beam (left) and 16, 32, 48, 64, 80, 90 and 98 mJy/beam (right). The negative contour is represented by a dotted line. The corresponding beam is shown in the lower left corner of each image.

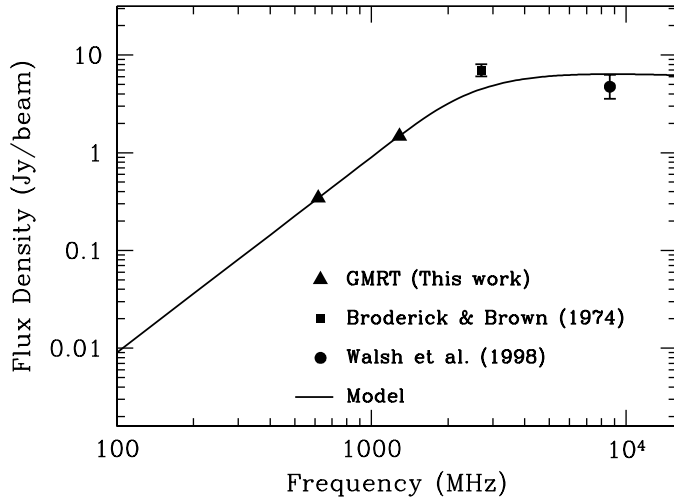


Figure 3. Free-free emission from the core S2 in G351.63-1.25 at low frequency radio wavebands. The observed measurements (with errorbars) are represented by symbols while the solid line shows the modeled flux densities. The filled triangles are measurements from GMRT while the filled circle and square represent flux density measurements from Walsh et al. (1998) and Broderick & Brown (1974), respectively. For GMRT measurements, the errors in flux are smaller than the symbol size used. These flux densities correspond to a beam size of $12''$.

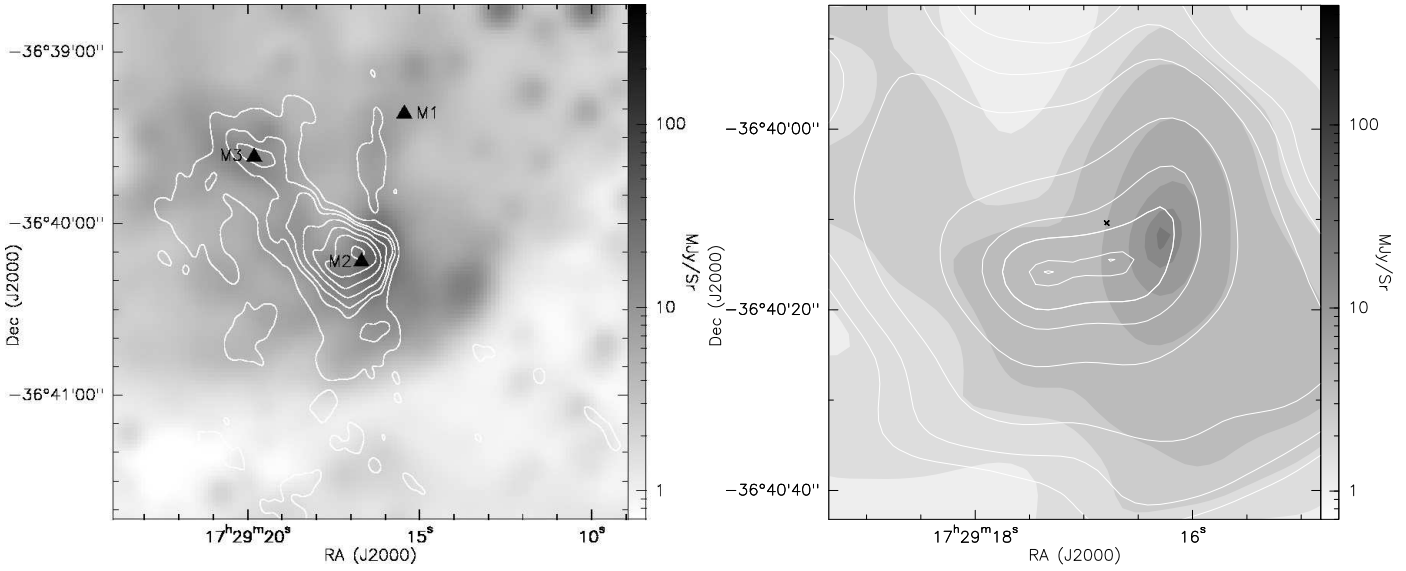


Figure 4. The grayscale represents 3.4 μm WISE image towards G351.63-1.25. (Left) The contours represent radio continuum emission from ionised gas at 1280 MHz with levels at 10, 30, 50, 100, 180, 250 and 300 mJy/beam where beam size is $\sim 7.0'' \times 3.6''$. The triangles represent MSX PSC sources. (Right) The contours represent emission from WISE for the central region at 4.6 μm with levels at 9.5, 11.3, 15, 30, 45, 52.5, 52.5, 58.7 and 59.7 MJy/Sr. The cross represents the position of S2.

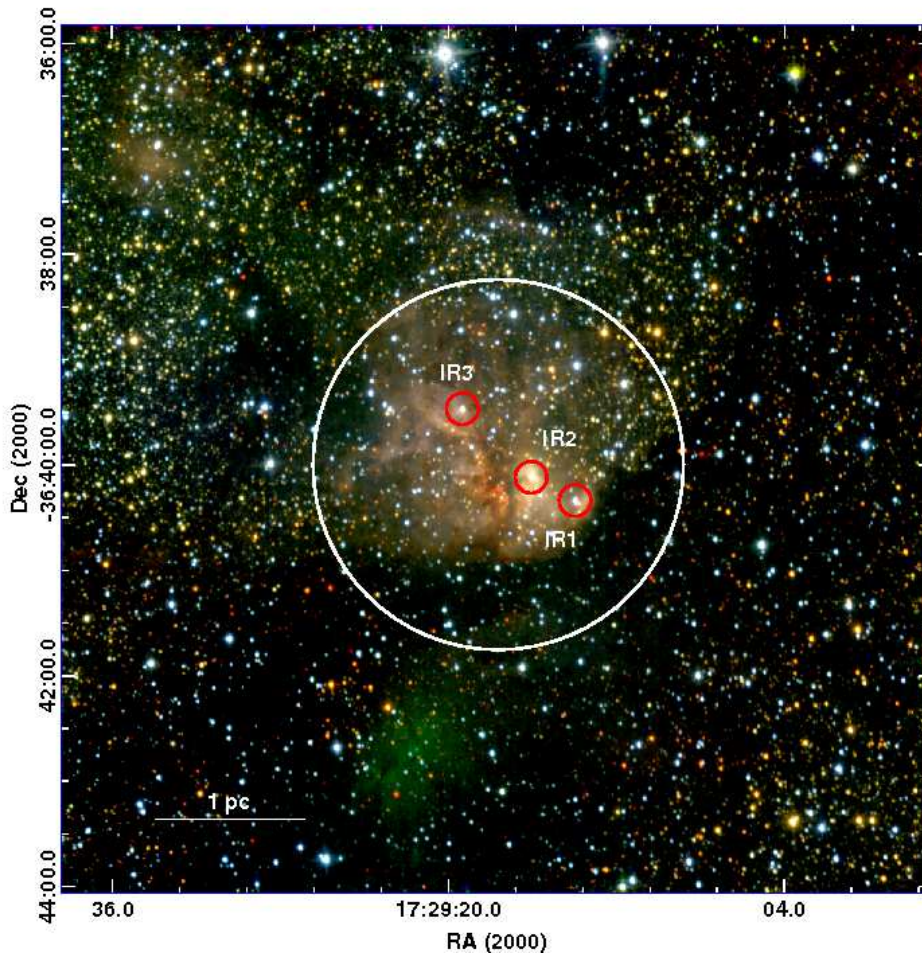


Figure 5. JHK_s colour-composite image of G351.63-1.25 where blue, green and red represent the emission in the J, H and K_s bands, respectively. The size of the image is 7.8' × 7.8'. North is up and east is towards the left. The circular region used for examining the embedded cluster is enclosed within the large white circle. Also shown are the three bright stellar objects (IR1, IR2, IR3) whose spectral types are known. (A color version of this figure is available in the online journal.)

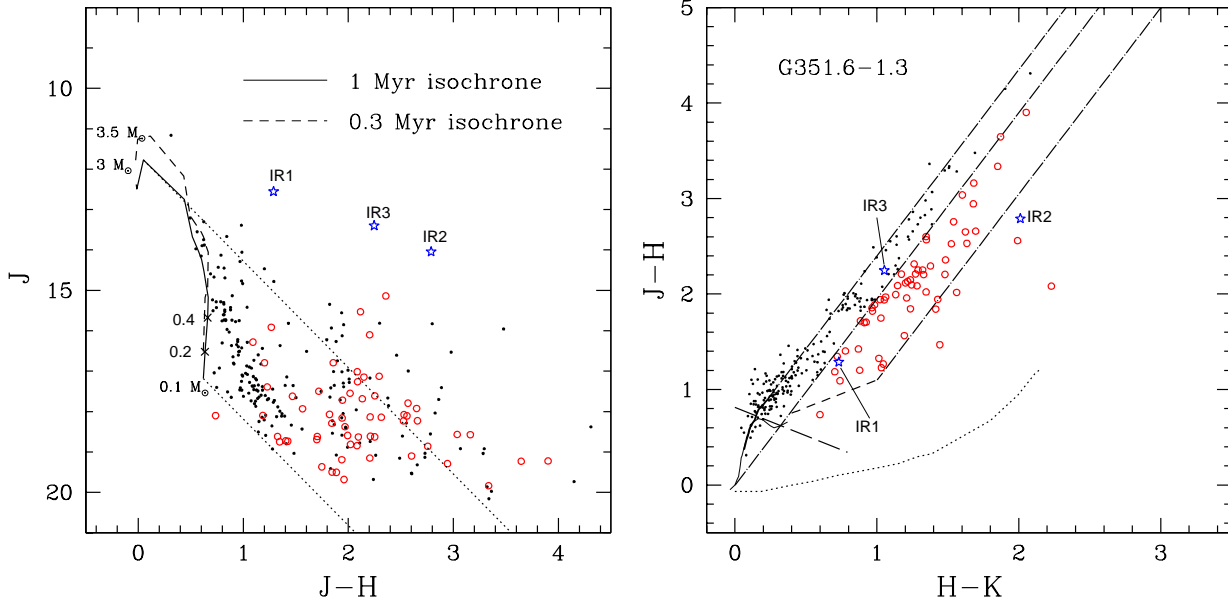


Figure 6. Colour-magnitude (left) and colour-colour (right) diagrams for the sources detected in all the three JHK_s bands using IRSF-SIRIUS in the region G351.63-1.25. Magnitudes of sources brighter than 11 mag in the K_s band were replaced with the corresponding magnitudes from the 2MASS PSC. The open circles represent the sources showing an infrared excess in the colour-colour diagram. The asterisks represent young stellar objects whose spectral type has been inferred based on other spectroscopic studies. The rest of the sources are represented by dots. In the colour-magnitude diagram, the solid and dashed curves represent model isochrones for pre-main-sequence stars from Palla & Stahler (1999) corresponding to 1 Myr and 0.3 Myr, respectively. The slanted dotted lines are the reddening vectors for 3 and 0.1 M_{\odot} pre-main-sequence stars corresponding to 1 Myr isochrone. The crosses denote the locations of 0.2 and 0.4 M_{\odot} on the 1 Myr isochrone. Sources that lie above the reddening vector for 3 M_{\odot} are likely luminous massive star candidates. In the colour-colour diagram, the loci of the main-sequence stars and giants are shown by the solid lines (thin and thick), respectively. The short-dashed and dotted lines represent the loci of classical T-Tauri stars and Herbig Ae/Be stars, respectively. The three parallel dash-dotted lines follow the reddening vectors of giants, main-sequence stars (or dwarfs) and T-Tauri stars. The long dashed line shown is drawn tangentially to the turn-off point of the main-sequence locus and used to estimate the reddening of the sources (see text for more details).

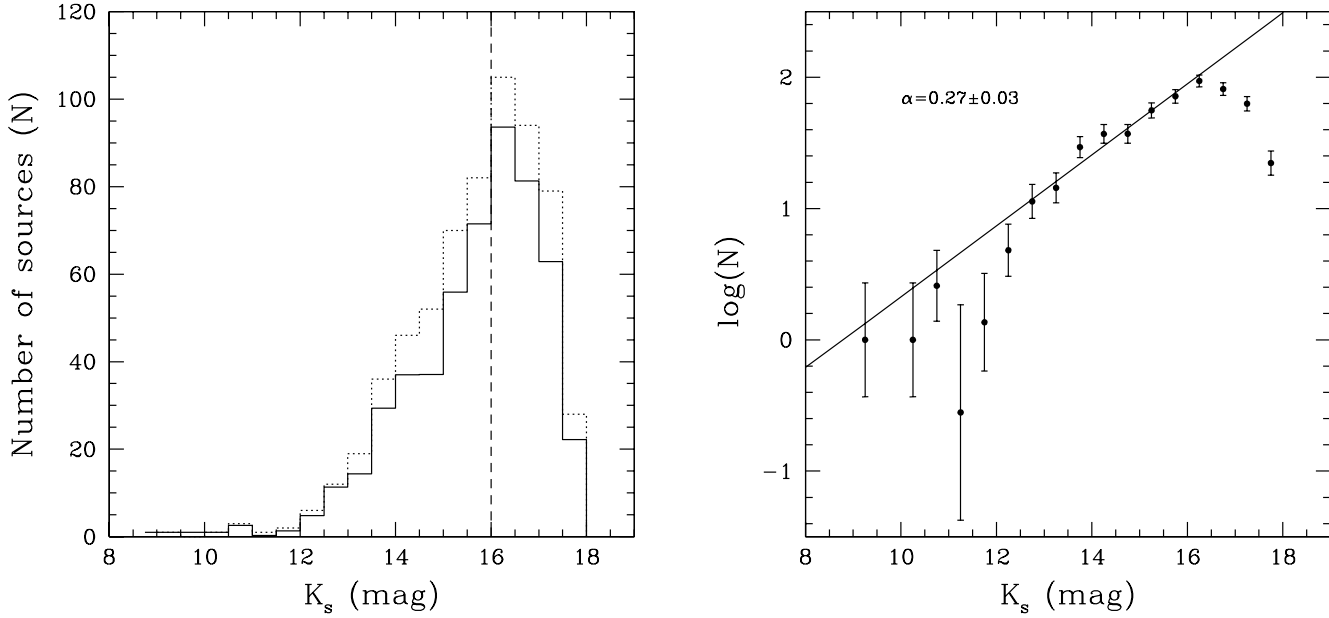


Figure 7. The corrected K_s -band luminosity function (KLF) for the embedded cluster associated with G351.63-1.25 is shown as a solid line histogram (left). The dotted line histogram is the luminosity function without correction for contamination (foreground and background sources) and the dashed vertical line represents the 90% completeness limit. The KLF is also shown as logarithm of number of stars (N) versus the K_s magnitude (right). The filled circles are the observed number of stars in a given magnitude bin while the error on this number is given by \sqrt{N} . The straight line is the least-square fit to the data points in the K_s magnitude range 11.5 – 16.0.

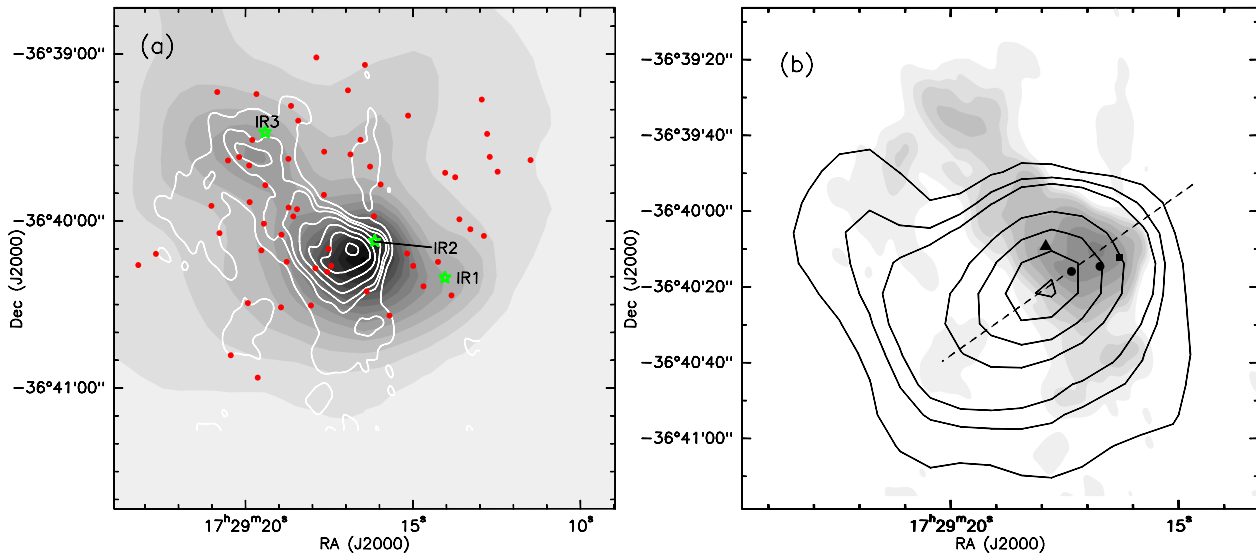


Figure 8. (a) Grayscale emission from warm dust (MSX $8 \mu\text{m}$) in the vicinity of G351.63-1.25 with levels ranging from $2.5 \times 10^{-7} \text{ Wm}^{-2}\text{Sr}^{-1}$ to $5 \times 10^{-4} \text{ Wm}^{-2}\text{Sr}^{-1}$ in steps of $1.8 \times 10^{-5} \text{ Wm}^{-2}\text{Sr}^{-1}$. The solid line contours represent the 1280 MHz radio continuum emission, the contour levels are same as those shown in Fig. 4 (left). The asterisks represent young stellar objects whose near-infrared spectral type has been inferred based on other spectroscopic studies and the circles represent infrared excess sources. (b) Grayscale is 1280 MHz radio emission, while the contours represent 1.2 mm emission with contour levels ranging from 0.5 to 14 Jy/beam in steps of 1.5 Jy/beam; beam is $24''$. The triangle represents the position of Class I methanol maser. The filled square and circles represent emission peaks at 3.4 and $4.6 \mu\text{m}$ from WISE, respectively. The dashed line represents the direction of thin flat molecular cloud (see text for more details).